coatings

MDPI

*Article*

# Water-Repellent Coatings on Corrosion Resistance by Femtosecond Laser Processing

**Zexu Zhao [1], Guoyun Luo [1], Manping Cheng [2] and Lijun Song [1,*]**

[1] State Key Laboratory of Advanced Design and Manufacturing for Vehicle Body, Hunan Provincial Key Laboratory of Intelligent Laser Manufacturing, Hunan University, Changsha 410082, China
[2] Research Institute of Automobile Parts Technology, Hunan Institute of Technology, Hengyang 421002, China
* Correspondence: ljsong@hnu.edu.cn

**Abstract:** Metal corrosion causes huge economic losses and major disasters every year. Inspired by the lotus leaf and nepenthes pitcher, the superhydrophobic surfaces (SHS) and the slippery liquid-infused porous surfaces (SLIPS) were produced as a potential strategy to prevent metal corrosion. However, how to prepare stable water-repellent coatings that can prevent the intrusion of corrosive ions remains to investigate. In this work, we first fabricated a micro/nano hierarchical structure on the aluminum surface by femtosecond laser processing. Then, the SHS was prepared on the above structure by fluorosilane modification. Finally, the SLIPS was fabricated on the SHS by coating lubricant. The morphology and wettability of the fabricated samples were evaluated by scanning electron microscopy and contact angle measurements. Furthermore, the corrosion resistance properties of SHS and SLIPS in simulated seawater were characterized by electrochemical measurements. From the comparison of the electrochemical parameters of different immersion times, both water-repellent coatings are effective in protecting the aluminum alloy from corrosion in simulated seawater due to reduced contact area between the metal substrate and corrosive solution. In comparison with the SHS, the SLIPS has a corrosion inhibition efficiency of up to 99.95% and it maintains long-term stability in the corrosive solution. This work also provides a promising method for the water-repellent coatings by femtosecond laser processing for metal corrosion prevention in practical industrial applications.

**Keywords:** femtosecond laser processing; corrosion resistance; superhydrophobic surface; SLIPS



**Citation:** Zhao, Z.; Luo, G.; Cheng, M.; Song, L. Water-Repellent Coatings on Corrosion Resistance by Femtosecond Laser Processing. *Coatings* **2022**, *12*, 1736. https://doi.org/10.3390/coatings12111736

Academic Editor: Mohamed Selim

Received: 18 October 2022
Accepted: 10 November 2022
Published: 13 November 2022



## 1. Introduction

Corrosion, as a natural process, causes huge economic losses and major disasters every year [1]. As a material widely used in industrial fields, although aluminum alloys naturally form oxide films in a dry and salt-free environment to prevent further corrosion, they are susceptible to corrosive ion attack in humid and salty environments [2], which will cause damage to equipment and limit the application of aluminum alloys. Hence, it is extremely important to have efficient anti-corrosion methods, which will also protect the industrial equipment and expand the application of aluminum alloys. There are various common anti-corrosion methods such as forming passivation layer [3], coating fabrication [4,5] and adding corrosion inhibitors [6], etc. However, they have many disadvantages: the passivation film is inherently hydrophilic and easy to crack, the traditional anti-corrosion coating is porous and its preparation process is environmentally unfriendly, corrosion inhibitors are highly toxic, and the coatings could not maintain long-term stability due to the poor adhesion to the aluminum surface. Therefore, it is necessary to develop a new environmentally friendly water-repellent coating fabrication strategy to achieve long-term stable corrosion resistance of aluminum alloys in corrosive environments.

Inspired by lotus leaf, superhydrophobic surfaces (SHS) have been reported for corrosion protection of metals due to their excellent water repellency [7–9]. The superhydrophobic behavior of the lotus leaves is determined by the micro/nano hierarchical structure and

low surface energy on its surface. The micro/nano hierarchical structure can easily trap the air layer to block the contact of the metal substrate and corrosive medium. Currently, there are many SHS fabricating technologies have been reported, such as electrodeposition [10], anodization [11], sol–gel processing [12], hydrothermal [13], chemical etching [14], laser processing [15], and so on [16,17]. Compared with other technologies, laser processing is highly efficient, easy to control and environmentally friendly, and it has been increasingly used in industry to fabricate micro/nano hierarchical structures [18]. The femtosecond laser features an extremely short laser–material interaction time compared with conventional lasers (ps, ns, quasi-continuous or continuous laser), which is far less than the time of heat transfer to the lattice (about 10 ps). The characteristics of femtosecond laser's "cold processing" determine that it will not bring no thermal cracks, thermal deformation and thick recast layers in the macro, but more abundant nanostructures in the micro (formed by phase explosion) [19]. Therefore, over the past two decades, the femtosecond laser has attracted the attention of researchers for the fabrication of various micro/nano structures for SHS of aluminum alloy [20–22]. However, there are few reports on corrosion resistance of SHS by femtosecond laser processing.

Inspired by nepenthes pitcher, slippery liquid-infused porous surfaces (SLIPS) have been reported [23]. There are three criteria for the fabrication of the SLIPS [24]. First, a micro/nano hydrophobic substrate is needed to stably adhere lubricant. Second, the lubricant must have low surface energy to ensure that it is not displaced by corrosive liquid. Third, the lubricant and corrosive liquid should be immiscible. The SLIPS, which consists of a film of lubricating liquid locked in the surface by a micro/nano structure, is a potential strategy instead of SHS to prevent metal corrosion. This is because the defect-free lubricant surface can repel immiscible liquids whose surface tension is greater than that of the lubricating oil. To the best of our knowledge, the corrosion resistance of SLIPS by femtosecond laser processing has not been studied.

Recently, some teams have reported that the corrosion resistance of metal substrates can be improved by laser treatment combined with other methods. For example, in the experiment of Tran et al., 316L stainless steel gained superhydrophobic characteristics after the treatment of ns laser and long-term atmospheric exposure, and its corrosive current was decreased from 0.72 to 0.29 $\mu A/cm^2$ [15]. Then, the team used femtosecond laser peening in combination with long-term atmospheric exposure to reduce the corrosive current of 2024-T3 aluminum alloy by 75% [25]. Ma et al. prepared the superhydrophobic surface on carbon steel with ns laser and fluorosilane, and obtained the lowest corrosive current of 0.16 $\mu A/cm^2$ [18]. By femtosecond laser and heat treatment, Guo et al. prepared superhydrophobic Al whose corrosive resistance efficiency is 41.4% [22]. Although there were previous research reports stating that the laser treatment can improve the corrosion resistance, the thermal cumulative damage, such as thermal cracking, thermal deformation, etc., brought by ns laser to metal substrates cannot be ignored. In addition, the corrosion resistance efficiency of the femtosecond laser still has much room for improvement despite avoiding the disadvantages of adopting the ns laser.

In the present work, the micro/nano hierarchical structures were fabricated on the surface of 1060 aluminum alloy by femtosecond laser processing. Then, the SHS was prepared on the above structure by chemical modification with fluorosilane. Finally, the lubricant perfluoropolyether was coated on the surface of the SHS to fabricate SLIPS. The performance of the corrosion resistance was evaluated using polarization curves and electrochemical impedance spectra in simulated seawater, while particular attention was paid on the stability of the water-repellent coatings. The results revealed that the SHS and SLIPS by femtosecond laser processing are effective strategies for improving the corrosion resistance of aluminum alloy. We hope that our strategies could aid the development of corrosion resistance of the water-repellent coatings in practical industrial applications.

## 2. Materials and Methods

### *2.1. Femtosecond Laser Processing*

We textured the surface of 1060 aluminum alloy (Al > 99.7 wt%). Before laser treatment, the samples with the size of 20 mm × 20 mm × 1 mm were fabricated via steel plate shearer, then successively polished with 800# and 2000# Silicon Carbide sandpaper and ultrasonically cleaned in ethanol, deionized water. The samples were processed by using a fiber femtosecond laser (Tangerine HP, Amplitude Systèmes, Bordeaux, France) at a laser wavelength of 1030 nm and laser power of 35 W, repetition rate (f) 175 kHz and pulse duration of 250 fs. The x-axis and y-axis motion of the femtosecond laser beam were achieved by a galvanometer scanner (IntelliSCAN III14, SCANLAB, Puchheim, Germany) with a 160 mm f-theta objective. The beam spot diameter is about 30 µm. The samples were processed by the typical line-by-line in the X and Y directions at a line pitch of 10 um. The laser power (P) and the scanning speed were set to 12.5 W and 200 mm/s. The single pulse energy € is 71.5 µJ calculated by $E = P/f$. The peak fluence of a Gaussian beam (F) is 20.2 J/cm$^2$ calculated by $F = 8E/(\pi{\omega_0}^2)$ [26], where $\omega_0$ is the spot diameter.

### *2.2. Fabrication Water-Repellent Coatings*

The samples were hydrophilic after femtosecond laser processing. In order to reduce its surface energy, it must be chemically modified by a low surface energy reagent. In our work, the laser prepared sample was immersed in 1% 1H,1H,2H,2H-perfluorooctyltriethoxysilane ethanol solution for 2 h at room temperature and then dried with warm air. The SLIPS was fabricated by dropping Perfluoropolyether (GPL105, Krytox, Wilmington, DE, USA) over the SHS, and then tilted at an angle of about 20° for more than 2 h to remove the excess lubricant from the sample surface. The schematic diagram of the femtosecond laser preparation process of water-repellent coatings in shown in Figure 1.

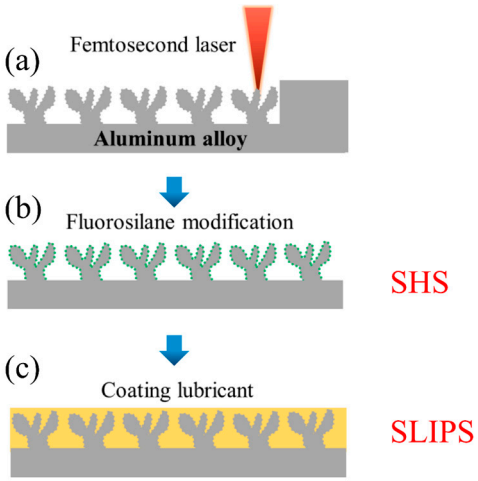


**Figure 1.** Schematic diagram of the preparation process: (**a**) Femtosecond laser processing; (**b**) Fluorosilane modification; (**c**) Infusion of the lubricant.

### *2.3. Morphology and Wettability*

The surface morphologies of untreated sample and laser textured sample were evaluated by scanning electron microscopy (SEM, TESCAN MIRA3 LMU, Brno, Czech Republic). The sample chemical compositions were characterized by the energy dispersive spectrum (Oxford X-Mx20, Oxford, UK) and X-ray photoelectron spectroscopy (XPS, ThermoFisher ESCALAB 250Xi, Waltham, MA, USA). The Untreated, SHS and SLIPS examined the static contact angle and sliding angle using the contact angle meter (Powereach, JC2000C1, Shanghai, China). The rolling angle is measured by manually rotating the measuring table very slowly and the process of droplet rolling down is recorded with a 100-frame camera. At the moment the droplet rolls down, the angle of the measuring table relative to the horizontal position at this time is recorded as the rolling angle. We carried out the measurement in at

least 5 different surface locations for each sample using a 6.5 µL distilled water droplet at room conditions of constant temperature of 22 °C and air humidity of around 50%.

### 2.4. Electrochemical Measurements

The electrochemical properties of the Untreated sample, SHS and SLIPS were studied using the Electrochemical workstation (Interface 1010E, Gamry, Philadelphia, PA, USA). The measurements were carried out at room temperature in the plate corrosion electrolytic cell (Gaossunion, Wuhan, China) with a saturated calomel electrode (SCE) as a reference electrode, and a 20 mm × 20 mm Pt mesh as a counter electrode. The electrolyte was a 3.5% NaCl solution as a simulated seawater. The working electrode contacted with the electrolyte through a 1 $cm^2$ circular area of a Teflon gasket. First, the samples were in the simulated seawater for 1 h in order to obtain relatively stable open circuit potential (OCP). The electrochemical impedance spectra (EIS) tests were obtained at frequencies ranging from $10^5$ to 0.2 Hz at OCP with a perturbation amplitude voltage of 10 mV. For the polarization curve test, the potential was scanned from −0.5 to +1.5 V versus the OCP at a scan rate of 1 mV/s.

## 3. Results and Discussion

### 3.1. Morphology and Composition

During femtosecond laser processing, the sample surfaces are ablated and plasma is formed, which is due to strong laser–matter interactions such as phase explosion and Coulomb explosion. When the energy density exceeds the ablation threshold of the metal, laser ablation forms the micro-scale structure on the surface. At the same time, the laser-induced plasma (includes atoms, clusters and particles) is partially deposited on the material surface. Finally, a micro/nano hierarchical structure containing micro-scale skeleton structures and redeposited nanoparticles attached to it is formed [27].

Figure 2 shows the surface topography of the aluminum alloy surface after femtosecond laser processing. The surface was textured to form a micro/nano hierarchical structure (Figure 2a,b). Its surface is covered with columnar structures of several microns to tens of microns. At the top of the columnar structure are densely distributed sub-micron clusters, which are formed by the deposition of nanoparticles of tens of nanometers (Figure 2d). This micro-nano hierarchical structure similar to the fractal structure provides a significantly large surface area for fluorosilane molecules or lubricating oils to adhere to. For the SLIPS construction, the microstructure can store lubricant, and the nanostructure can absorb lubricant by capillary action. It is particularly noteworthy that the micro/nano hierarchical structure of the entire sample surface is prepared within 7 min, no additional consumables or chemical reagents are required for the whole femtosecond laser processing, and the electrical energy cost is about 0.03 dollars (calculated based on 3.5 kW equipment power). All of those show that the femtosecond laser processing is an efficient, low-cost, environmentally friendly one-step method to prepare large-area controllable micro/nano hierarchical structures. In fact, if the polygon scanner with scanning speed up to hundreds of meters per second can be used to perform femtosecond laser processing, the current processing speed can be thousands of times faster to meet the actual industrial needs.

Figure 2c shows the EDS of the superhydrophobic surface. There are Si, C, F and O elements, which are the major elements of fluorosilane. It reveals the low surface energy fluorosilane was grafted to the surface of the aluminum alloy after femtosecond laser processing. For accurate detection of the SHS component, XPS was utilized to test the chemical composition of the sample after fluorosilane modification. As shown in Figure 3a, the XPS survey spectrum shows the presence of F, O, C, Si and Al on the SHS surface. We can infer that fluorosilane adheres to the surface of the substrate. In order to obtain more information about the SHS surface component, we tested the high-resolution XPS data for Al 2p, C 1s and F 1s. As shown in Figure 3b, the binding energy of the Al 2p peak is found to be 75.0 eV, which is assigned to O-Al-O($Al_2O_3$) bonding [28]. It indicates that there is only $Al_2O_3$ on the superhydrophobic surface after femtosecond laser processing, and no

pure aluminum exists. Figure 3c shows the high resolution of C 1s. It can be resolved into five different components, including -$CF_3$ (293.55 eV), -$CF_2$ (291.26 eV), $CH_2$-$CF_2$ (290.0 eV), C-O (285.6 eV), C-C (284.6 eV) [29]. The -$CF_3$, -$CF_2$ and $CH_2$-$CF_2$ components were thought of as the characteristics of fluorosilane molecules, which demonstrated that the textured aluminum was well modified by fluorosilane molecules. As shown in Figure 3d, the strong peak at 688.5 eV corresponded to F 1s, which is attributed to the F–C covalent bond [30]. Therefore, the SHS is successfully modified by a low surface energy reagent on the micro/nano hierarchical structure by femtosecond laser processing after immersion in an ethanol solution of fluorosilane.

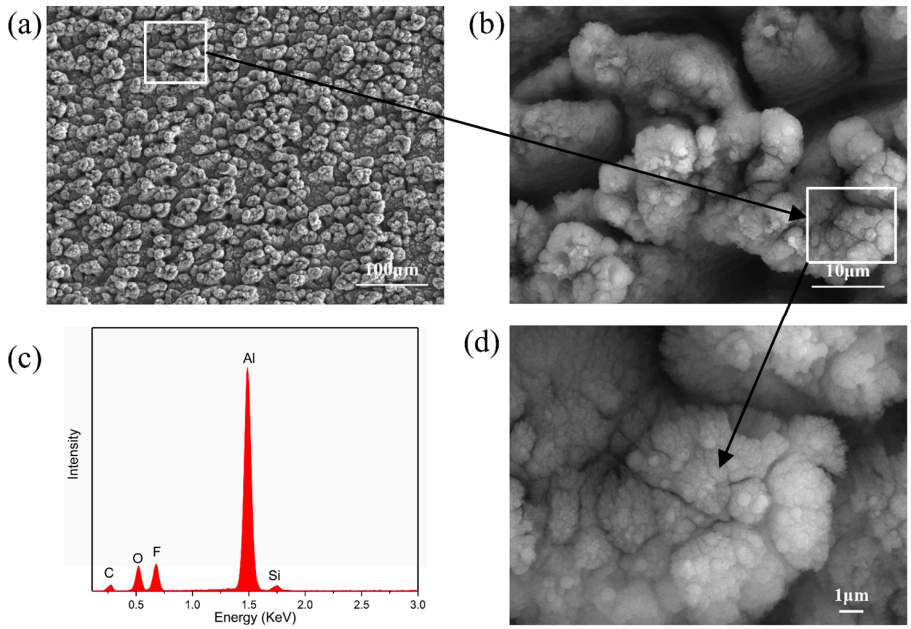


**Figure 2.** (**a**,**b**,**d**) scanning electron microscopy (SEM) microstructure of laser processing; (**c**) Energy dispersive spectrum (EDS) of the superhydrophobic surface.

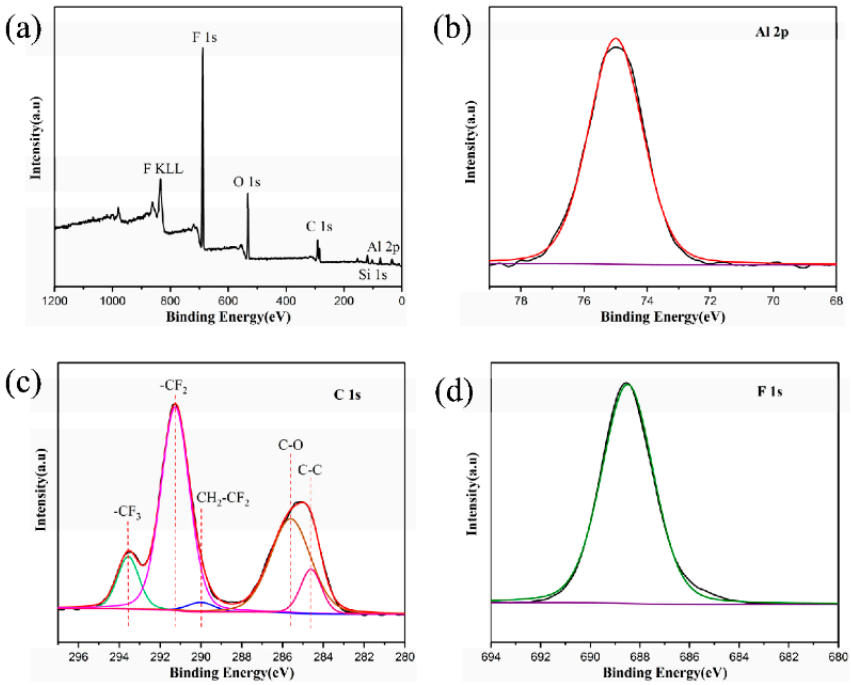


**Figure 3.** XPS spectra of the SHS: (**a**) XPS survey spectra; (**b**) high resolution of Al 2p; (**c**) high resolution of C 1s; (**d**) high resolution of F 1s.

### 3.2. Wettability

Figure 4 shows the optical photographs of 6.5 µL water droplets on the three samples (Untreated, SHS, SLIPS). As shown in Figure 4a, the Untreated sample surface shows hydrophilicity with the contact angle (CA) of 65° ± 0.5°. After fluorination by fluorosilane, the SHS sample surface exhibits superhydrophobic property with the CA of 152° ± 1° (Figure 4b) and the sliding angle (SA) of 3° ± 1° (Figure 4c). The low rolling angle indicates the low adhesion of SHS, greatly decreasing the adhesion of corrosive solutions, pollutants, or microorganisms. After lubrication by Perfluoropolyethe on the SHS, the lubricating oil which replaces the air layer penetrates into the columnar microstructure, and it is tightly adsorbed on the nanostructure through capillary force and van der Waals force. The SLIPS sample surface exhibits a slippery property with the SA of 2.5° (Figure 4e). It indicates that the lubricating layer forms over the laser textured surface.

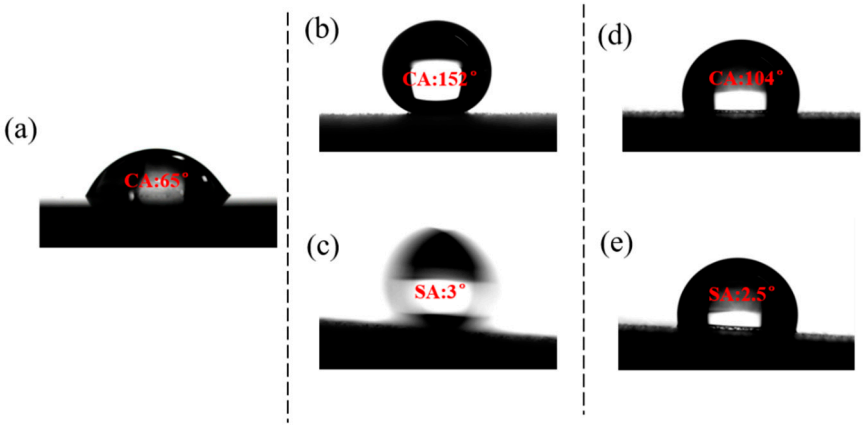


**Figure 4.** Wettability of the aluminum alloy: (**a**) CA of Untreated sample; (**b**,**c**) CA and SA of SHS sample, respectively; (**d**) CA and (**e**) SA of SLIPS sample, respectively.

There exist two models (the Wenzel model [31] and the Cassie–Baxter model [32]) to describe surface wettability. For superhydrophobic surface, the CA can be calculated by the Cassie–Baxter model:

$$cos\theta_r = f_1 cos\theta_0 - f_2 \quad (1)$$

where $\theta_r$ (152°) is the CA of the rough surface after laser processing, $\theta_0$ (65°) is the CA of the untreated smooth surface, $f_1$ is the area fraction of the solid–liquid interface, $f_2$ is the area fraction of the air-liquid interface, and $f_1 + f_2 = 1$. The solid–liquid contact radio $f_1$ is calculated to be 0.0823. It means that there are only 8.23% areas of the liquid contacted with the superhydrophobic surface, and the remaining 91.77% areas are air layer contacted with water. The surface wettability confirmed that the micro/nano hierarchical structures successfully captured the air layer, which blocks the intrusion of corrosive solution.

### 3.3. Corrosion Resistance

Figure 5 shows the polarization curves of the Untreated sample, SHS and SLIPS, which were immersed in the simulated seawater for 1 h. Table 1 shows the characteristic parameters obtained from polarization curves (Figure 5). The corrosion potential of Untreated sample, SHS and SLIPS are −0.744, −1.06, −1.16 V, respectively. The corrosion current density of Untreated sample is $1.084 \times 10^{-6}$ A/cm$^2$. After femtosecond laser processing and chemical modification, the corrosion current density of SHS decreases to $1.06 \times 10^{-7}$ A/cm$^2$. The reduction (90.22%) of current density is close to the surface air–liquid contact ratio (91.77%), indicating that the air layer of SHS reduces the corrosion rate and protects the aluminum alloy from corrosion. After coating lubricant, the corrosion current density of SLIPS further decreases to $1.44 \times 10^{-9}$ A/cm$^2$, which is ca.3 and ca.2 orders of magnitude lower than that of Untreated sample and SHS, respectively. This means that the insulating lubricant almost completely isolates the corrosive solution from the metal

substrate. As the potential gradually increases, pitting starts at −0.332 V for the SHS, after which the corrosion current rises rapidly and converges to that of the Untreated sample. The pitting potential of the SLIPS is lower than that of the SHS at −0.134 V, implying a better resistance to pitting. The sharp fluctuation of the polarization curve after the onset of pitting is due to the spontaneous filling of the pitting by the nearby lubricant preventing further expansion of pitting. These results indicate that the SHS and SLIPS both have good performance in preventing aluminum alloy from the simulated seawater in a short time.

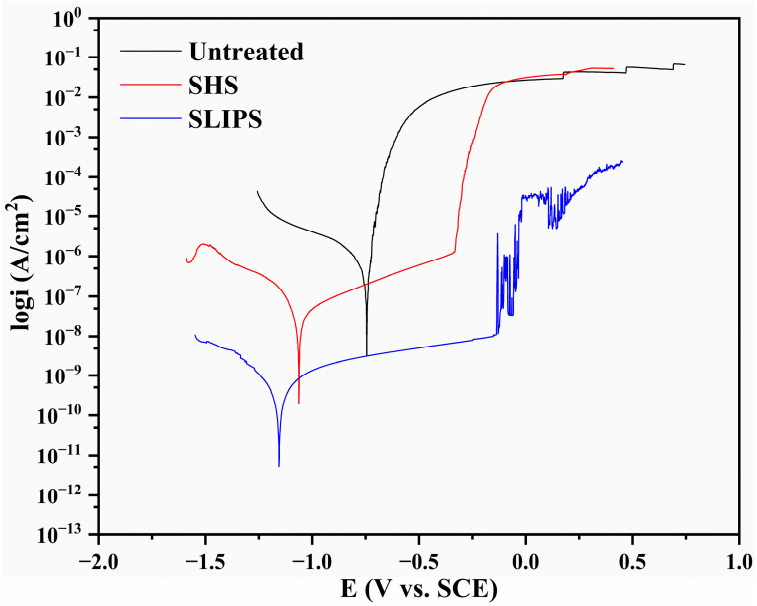


**Figure 5.** Polarization curves after immersion in simulated seawater for 1 h.

**Table 1.** The characteristic parameters obtained from polarization curves after immersion in simulated seawater for 1 h.

| Sample | $E_{corr}$ (V vs. SCE) | $I_{corr}$ (A/cm$^2$) | $E_{pit}$ (V vs. SCE) | $\eta_{pc}$ (%) |
|---|---|---|---|---|
| Untreated (1 h) | −0.744 | $1.084 \times 10^{-6}$ | / | / |
| SHS (1 h) | −1.06 | $1.06 \times 10^{-7}$ | −0.332 | 90.22% |
| SLIPS (1 h) | −1.16 | $1.44 \times 10^{-9}$ | −0.134 | 99.87% |

The corrosion inhibition efficiency ($\eta_{pc}$) can be calculated from the polarization curve, as shown in the following equation:

$$\eta_{pc}(\%) = (1 - \frac{I^0_{corr}}{I_{corr}}) \times 100 \quad (2)$$

where $I^0_{corr}$ is the corrosion current of the untreated sample, $I_{corr}$ is the corrosion current of the SHS or SLIPS.

To further explore the corrosion resistance of SHS and SLIPS, the electrochemical impedance spectra (EIS) were tested after the open circuit potential test. As shown in Figure 6, the EIS plots of the Untreated sample, SHS and SLIPS were obtained after immersion in 3.5% NaCl solution for 1 h. The Nyquist plots (Figure 6a) show that the semicircle diameter of SLIPS is several MΩ·cm$^2$, the semicircle diameter of SHS is tens of kΩ·cm$^2$ and the Untreated sample is several kΩ·cm$^2$. Figure 6c shows the $|Z|$ of SLIPS and SHS is ca.3 and ca.1 orders of magnitude higher than that of the Untreated sample in all frequencies. The result here is consistent with the polarization curves and the Nyquist plots.

When the samples were immersed in the solution, its electrochemical behavior which is similar to an electronic circuit, can be simulated by the equivalent circuit. Figure 7 shows

two kinds of equivalent circuits for fitting EIS plots. The first one, $R_s(Q_f(R_f(Q_{dl}R_{ct})))$, is for the Untreated sample in Figure 7a, and the second one, $R_s(Q_f(R_f(Q_{dl}(R_{ct}W))))$, is for SHS and SLIPS in Figure 7b. In the equivalent circuits, $R_s$ is the 3.5% NaCl solution resistance, $R_f$ represents the resistance of the anti-corrosion layer (corrosion product, air or lubricant), $R_{ct}$ means the charge-transfer resistance. W is the Warburg resistance. $Q_f$ and $Q_{dl}$ are the constant phase elements modeling capacitance of the anticorrosion layer and double electrode layer, respectively. The impedance of the constant phase element (CPE) is given as the following equation:

$$Z_{CPE} = \frac{1}{Y_0(j\omega)^n} \tag{3}$$

where $j$ is an imaginary unit and $\omega$ is an angular frequency ($\omega = 2\pi f$), $Y_0$ stands for frequency-independent real constant, and n presents the constant phase element exponent ($0 < n \leq 1$, $n = 1$ means CPE is "pure capacitance").

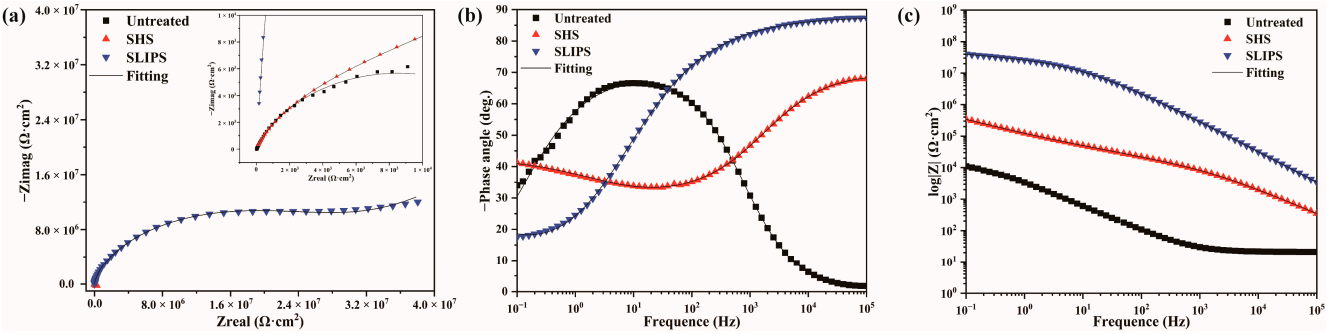


**Figure 6.** EIS after immersion in simulated seawater for 1 h: (**a**) Nyquist plots; Bode plots of (**b**) phase angle vs. Frequency; and (**c**) $|Z|$ vs. Frequency for the three samples.

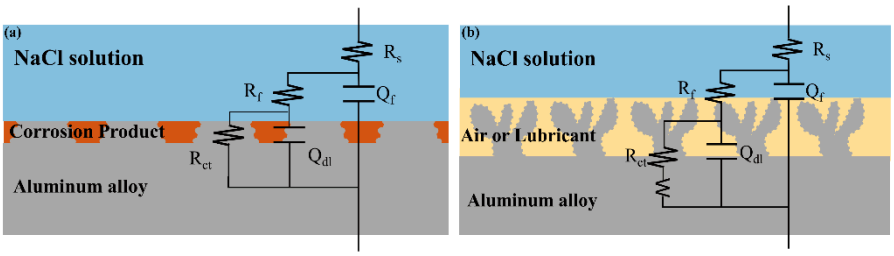


**Figure 7.** Equivalent circuits for analyzing EIS plots. (**a**) Untreated sample; (**b**) SHS and SLIPS.

The capacitance ($C$) of the anti-corrosion layer and double electrode layer is calculated by the following equation [25,33]:

$$C = \left(Y_0 R^{1-n}\right)^{\frac{1}{n}} \tag{4}$$

where $R$ is the resistance of the specific group, $Y_0$ and n are the CPE parameter and exponent, respectively.

Table 2 shows the electrochemical parameters obtained from EIS simulation with equivalent circuit after immersion in 3.5% NaCl solution for 1 h (Figure 6). The charge-transfer resistance ($R_{ct}$) of Untreated sample, SHS and SLIPS were $1.75 \times 10^4$, $9.21 \times 10^4$, $3.65 \times 10^7$ $\Omega \cdot cm^2$, respectively. The inhibition efficiencies ($\eta_{EIS}$) of SHS and SLIPS are 80.99%, 99.95%, respectively. The $R_{ct}$ and the $\eta_{EIS}$ indicated that both water-repellent coatings had good corrosion resistance.

Generally, the inhibition efficiency ($\eta_{EIS}$) can be calculated from the EIS results, as shown in the following equation [34]:

$$\eta_{EIS}(\%) = (1 - \frac{R_{ct}^0}{R_{ct}}) \times 100 \tag{5}$$

where $R_{ct}^{0}$ is the charge-transfer resistance of the untreated aluminum alloy substrate, and $R_{ct}$ is the charge-transfer resistance of the obtained SHS or SLIPS.

**Table 2.** Electrochemical parameters obtained from EIS simulation with equivalent circuit after immersion in simulated seawater for 1 h.

| Parameter | Untreated | SHS | SLIPS |
|---|---|---|---|
| $R_s$ ($\Omega \cdot cm^2$) | 21.03 | 15.65 | 14.7 |
| $Y_f$ ($S \cdot cm^{-2} \cdot sn$) | $3.026 \times 10^{-5}$ | $8.409 \times 10^{-8}$ | $6.23 \times 10^{-10}$ |
| $n_f$ | 0.8633 | 0.7806 | 0.9773 |
| $C_f$ ($F \cdot cm^{-2}$) | $1.0934 \times 10^{-5}$ | $1.17324 \times 10^{-8}$ | $4.9616 \times 10^{-10}$ |
| $R_f$ ($\Omega \cdot cm^2$) | 74.39 | 10780 | 88940 |
| $Y_{dl}$ ($S \cdot cm^{-2} \cdot s^n$) | $4.207 \times 10^{-5}$ | $2.34 \times 10^{-6}$ | $5.712 \times 10^{-9}$ |
| $n_{dl}$ | 0.641 | 0.4649 | 0.5036 |
| $C_{dl}$ ($F \cdot cm^{-2}$) | $3.54 \times 10^{-5}$ | $3.99 \times 10^{-7}$ | $1.22 \times 10^{-9}$ |
| $R_{ct}$ ($\Omega \cdot cm^2$) | $1.75 \times 10^{4}$ | $9.21 \times 10^{4}$ | $3.65 \times 10^{7}$ |
| $Z_w$ ($\Omega^{-1} \cdot s^{0.5} \cdot cm^{-2}$) | / | $1.44 \times 10^{-6}$ | $8.98 \times 10^{-8}$ |
| $\eta_{EIS}$ (%) | / | 80.99 | 99.95 |

In order to study the long-term corrosion resistance of SHS and SLIPS, the polarization curves of the Untreated sample, SHS and SLIPS were tested after immersion in simulated seawater for 24 h (Figure 8). The corrosion potential of the Untreated sample, SHS and SLIPS are −0.825, −1.02, −1.12 V, respectively. Table 3 shows the characteristic parameters obtained from polarization curves after immersion for 24 h (Figure 8b). The corrosion current density values of Untreated sample, SHS are reduced to $1.56 \times 10^{-7}$, $2.97 \times 10^{-8}$ A/cm$^2$, respectively. This result may be caused by the formation and thickening of porous corrosion products [35]. The reduction of the corrosion current of the SHS relative to the Untreated sample is 80.96%, which is lower than 90.22% immersion for 1 h. Meanwhile, the pitting potential drops to −0.455 V. The changed reductions demonstrate that the air layer lost over time. The corrosion current density of SLIPS slightly decreased from $1.44 \times 10^{-9}$ to $1.7 \times 10^{-9}$ A/cm$^2$ and the pitting potential decreases slightly from −0.134 to −0.190 V, which shows the slow loss of lubricant over time. Although both air layer and lubricant are lost over time, both water-repellent coatings still have great corrosion resistance.

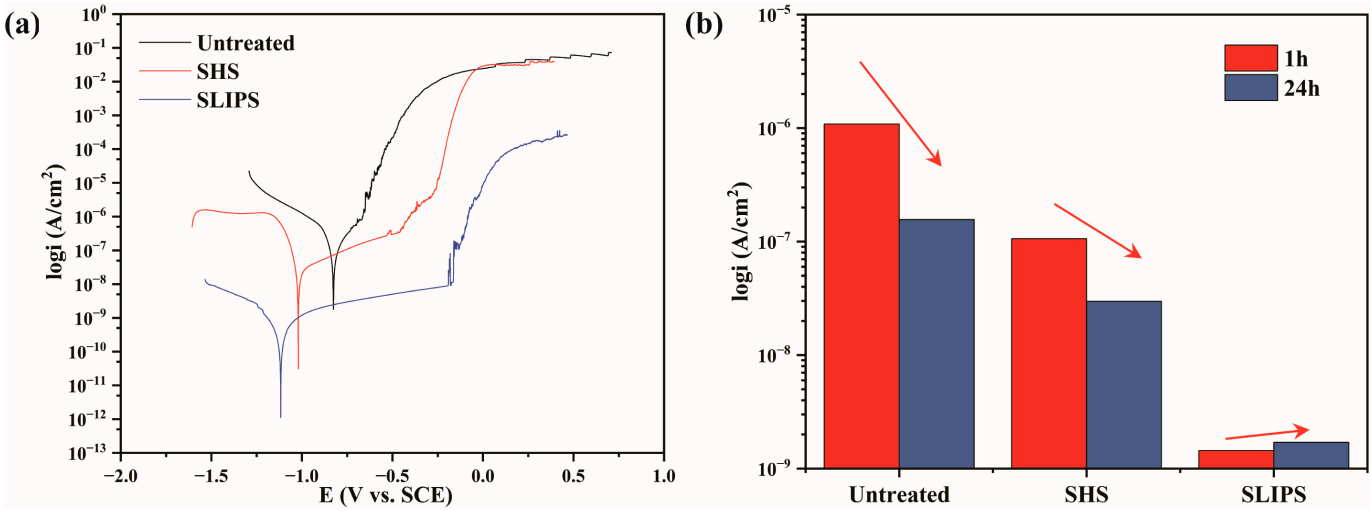


**Figure 8.** (**a**) Polarization curves after immersion in simulated seawater for 24 h; (**b**) Contrast for corrosion current density.

The EIS was also tested after being immersed in simulated seawater for 24 h. The Nyquist plots (Figure 9a) show that the semicircle diameter of SLIPS is still several M

ohms, but the semicircle diameter of SHS and Untreated sample increased by an order of magnitude. The Bode-$Z_{imag}$ (Figure 9c) shows the absolute impedance $|Z|$ values of Untreated sample and SHS increase several times, and the $|Z|$ of SLIPS is almost constant. These results here are consistent with the changed corrosion currents. Table 4 shows the electrochemical parameters obtained from EIS simulation with equivalent circuit after immersion in simulated seawater for 24 h. The charge-transfer resistance ($R_{ct}$) of Untreated sample, SHS and SLIPS were $5.69 \times 10^4$, $3.04 \times 10^5$, $3.70 \times 10^7$ $\Omega \cdot cm^2$, respectively. The inhibition efficiencies ($\eta_{EIS}$) of SHS and SLIPS are calculated as 81.28%, 99.84%, respectively. After immersion for 24 h, the $R_{ct}$ of SHS was 3 times that of immersion for 1 h, and the $R_{ct}$ of SLIPS was almost unchanging. Meanwhile, the $\eta_{EIS}$ of SHS increased a little from 80.99% to 81.28%, and the $\eta_{EIS}$ of SLIPS was reduced by approximately 0.1% from 99.95% to 99.84%. Therefore, both SHS and SLIPS had better corrosion resistance for a long time, and the SLIPS was more stable over time.

**Table 3.** The characteristic parameters obtained from Polarization curves after immersion in simulated seawater for 24 h.

| Sample | $E_{corr}$ (V vs. SCE) | $I_{corr}$ (A/cm$^2$) | $E_{pit}$ (V vs. SCE) | $\eta_{pc}$ (%) |
|---|---|---|---|---|
| Untreated (24 h) | −0.825 | $1.56 \times 10^{-7}$ | −0.659 | / |
| SHS (24 h) | −1.02 | $2.97 \times 10^{-8}$ | −0.455 | 80.96% |
| SLIPS (24 h) | −1.12 | $1.7 \times 10^{-9}$ | −0.190 | 98.91% |

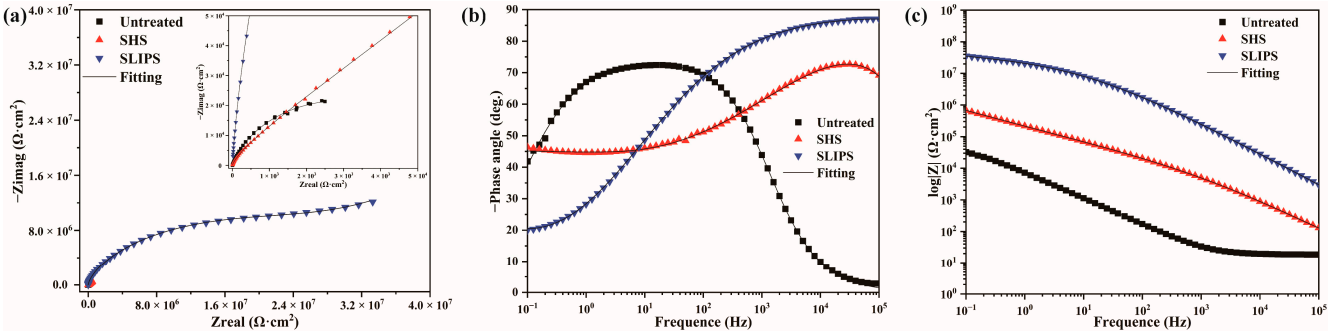


**Figure 9.** EIS after immersion in simulated seawater for 24 h: (**a**) Nyquist plots; Bode plots of (**b**) phase angle vs. Frequency and (**c**) $|Z|$ vs Frequency for the three samples.

**Table 4.** Electrochemical parameters obtained from EIS simulation with equivalent circuit after immersion in simulated seawater for 24 h.

| Parameter | Untreated | SHS | SLIPS |
|---|---|---|---|
| $R_s$ ($\Omega \cdot cm^2$) | 18.49 | 25.51 | 18.16 |
| $Y_f$ ($S \cdot cm^{-2} \cdot s^n$) | $2.50 \times 10^{-5}$ | $2.083 \times 10^{-8}$ | $7.342 \times 10^{-10}$ |
| $n_f$ | 0.8479 | 0.9553 | 0.9751 |
| $C_f$ ($F \cdot cm^{-2}$) | $1.64 \times 10^{-5}$ | $8.77 \times 10^{-9}$ | $5.93 \times 10^{-10}$ |
| $R_f$ ($\Omega \cdot cm^2$) | 3769 | 25.96 | 316700 |
| $Y_{dl}$ ($S \cdot cm^{-2} \cdot s^n$) | $6.51 \times 10^{-6}$ | $1.49 \times 10^{-10}$ | $5.712 \times 10^{-9}$ |
| $n_{dl}$ | 0.5853 | 0.5065 | $1.008 \times 10^{-10}$ |
| $C_{dl}$ ($F \cdot cm^{-2}$) | $3.22 \times 10^{-6}$ | $6.90 \times 10^{-7}$ | $3.64 \times 10^{-9}$ |
| $R_{ct}$ ($\Omega \cdot cm^2$) | $5.69 \times 10^4$ | $3.04 \times 10^5$ | $3.702 \times 10^7$ |
| $Z_w$ ($\Omega^{-1} \cdot s^{0.5} \cdot cm^{-2}$) | / | $3.84 \times 10^{-7}$ | $1.021 \times 10^{-7}$ |
| $\eta_{EIS}$ (%) | / | 81.28 | 99.84 |

Moreover, in order to further reveal the long-term stability mechanism of the SHS and SLIPS in the corrosion solution, the total interfacial energy (E) was discussed. When the SHS is immersed in the NaCl solution, the substrate, the air layer and the solution are

in contact with each other in pairs. The total interfacial energy of the SHS ($E_{SHS}$) can be calculated by [13]:

$$E_{SHS} = \gamma_w(1 - f - fcos\theta_w)A + \gamma_s rA \quad (6)$$

where, $A$, $\gamma_s$ and $r$ are the surface area, interfacial tension and roughness factor of the SHS, respectively. The surface tension of water ($\gamma_w$) is 72.1 mN/m. the water contact angle ($\theta_w$) on the smooth superhydrophobic surface is 104° (Figure 10a). The solid–liquid contact radio ($f$) was calculated as 0.0823 by Equation (1). Thus, Equation (6) can be written as:

$$E_{SHS} = 67.60A + \gamma_s rA \quad (7)$$

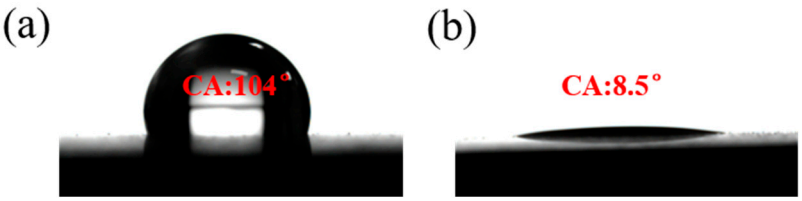


**Figure 10.** (**a**) Water CA ($\theta_w$) on the smooth superhydrophobic surface; (**b**) CA of lubricant ($\theta_0$ ) on smooth surface modified fluorosilane.

When the SLIPS is immersed in the NaCl solution, the substrate, lubricating oil and the solution are in contact in sequence. The total interfacial energy of the SLIPS ($E_{SLIPS}$) can be calculated by [13]:

$$E_{SLIPS} = \gamma_s rA - rA\gamma_0 cos\theta_0 + \gamma_{ow}A \quad (8)$$

where A, $\gamma_s$ and r are the surface area, interfacial tension and roughness factor of the solid substrate, respectively. The surface tension of the lubricant ($\gamma_0$) is 17.2 mN/m, and the lubricant–water interfacial tension ($\gamma_{ow}$) is 55.7 mN/m. The CA of the lubricant ($\theta_0$) on the untreated smooth surface chemically modified by fluorosilane is 8.5°(Figure 10b). Thus, Equation (8) can be written as:

$$E_{SLIPS} = \gamma_s rA - 17.01rA + 55.7A \quad (9)$$

When the corrosive solution completely replace the air layer of the SHS (or the lubricant of the SLIPS), the total surface energy in the steady state can be obtained by Equation (10) combined with the Young's equation:

$$E_{cs} = \gamma_s rA - \gamma_w rAcos\theta_w = \gamma_s rA + 17.44\, rA \quad (10)$$

The long-term stability of the SHS and the SLIPS can be calculated by the following equations:

$$E_{SHS} = E_{cs} - E_{SHS} = 17.44\, rA - 67.60A \quad (11)$$

$$\Delta E_{SLIPS} = E_{cs} - E_{SLIPS} = 34.44\, rA - 55.7A \quad (12)$$

When the total interfacial energy difference $\Delta E$ is greater than 0, the SHS and SLIPS can maintain water repellency. According to the Equations (11) and (12), we can infer that the SHS can maintain superhydrophobicity when the roughness factor $r$ is greater than 3.88, and the SLIPS can maintain the slippery property in the case when $r$ is greater than 1.62. For the SHS and the SLIPS processed with the same femtosecond laser parameters, the surface roughness factor r values are the same due to the same micro/nano hierarchical structure. This means that $\Delta E_{SLIPS}$ is always much higher than the $\Delta E_{SHS}$. This result theoretically discusses the long-term stability of the SHS and SLIPS immersion in corrosion solution, and at the same time proves that SLIPS have better corrosion resistance stability.

Figure 11 shows the SEM images of the Untreated sample, SHS and SLIPS after electrochemical measurement immersion in simulated seawater for 24 h. Before the SEM

test, all samples were ultrasonically cleaned with acetone solution for 5 min to remove corrosion products. As shown in Figure 11a–c, the Untreated sample was covered with hundreds of micrometers of corrosion pits in the circular test area. As shown in Figure 11d–f, the SHS was covered with a smaller scale of about tens of micrometers, but more corrosion pits in the circular test area. The result demonstrated that the SHS effectively improves surface corrosion resistance. As shown in Figure 11g–i, there is almost no corrosion pit on the SLIPS even on the scale of tens of microns. Furthermore, it can be seen from Figure 11i that the lubricant remains attached to the micro/nano structures after the ultrasonic acetone cleaning, which indicates that the rich nanostructures prepared by the femtosecond laser processing greatly improve the adhesion to lubricant and avoid the problems of poor adhesion and fragile paint film of traditional coatings. Meanwhile, the result exhibited that the SLIPS almost completely prevents the occurrence of corrosion. Both water-repellent coatings exhibit excellent corrosion resistance in corrosive solution, and the SLIPS is more effective in preventing chloride ions from invading the substrate.

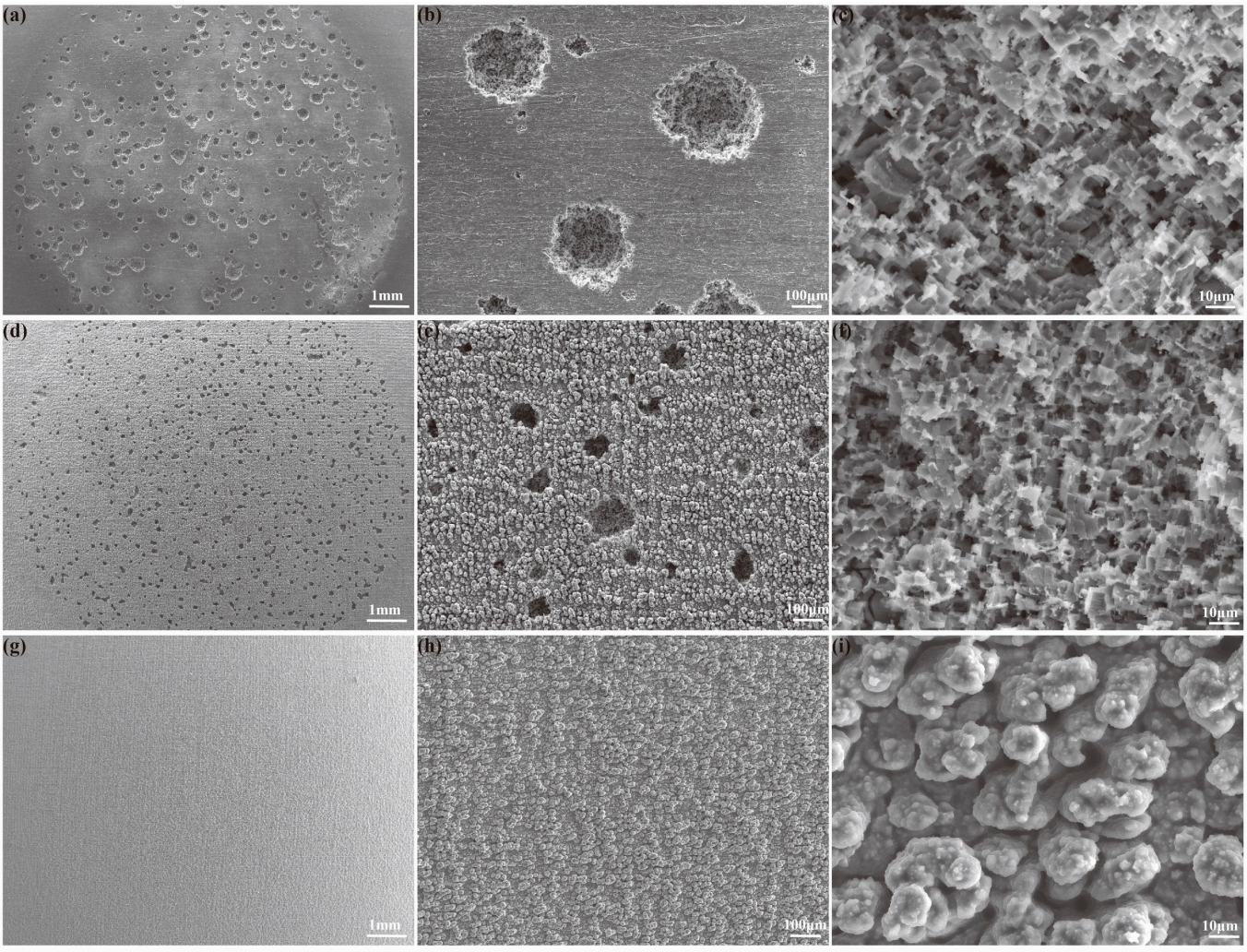


**Figure 11.** SEM images after electrochemical measurement immersion in simulated seawater for 24 h: (**a**–**c**) Untreated sample; (**d**–**f**) SHS; (**g**–**i**) SLIPS.

## 4. Conclusions

The two kinds of water-repellent coatings with micro/nano hierarchical structures were successfully fabricated by femtosecond laser processing. The SHS was prepared on the above structure by chemical modification with low surface energy fluorosilane. The SLIPS was fabricated on the SHS by coating lubricant perfluoropolyether. The SHS exhibits high water repellency with contact water angle of 152° by constructing an air layer. The

SLIPS presents slippery properties for water droplets with low sliding angle as a result of the lubricant layer replacing the air layer.

The corrosion current density of SHS and SLIPS was ca.1 and ca.3 orders of magnitude lower than that of the Untreated sample. It demonstrated that both samples had good anti-corrosion performance. In the long-term immersion, from the comparison of corrosion current density, charge-transfer resistance and electrochemical morphology, the lubricant was more effective than the air layer in terms of protecting the aluminum alloy from corrosion in simulated seawater. Although this research work proved that the SHS and SLIPS prepared by the femtosecond laser processing of aluminum alloy possess excellent corrosion resistance, the properties of the water-repellent coatings still need to be further studied, including their mechanical stability (such as friction and wear), chemical stability (such as oily pollutants), biofouling and processing efficiency optimization (such as parallel processing), before being applied in the industry.

**Author Contributions:** Conceptualization, Z.Z. and G.L.; methodology, Z.Z. and G.L.; software, Z.Z.; validation, Z.Z., G.L. and M.C.; formal analysis, Z.Z.; investigation, M.C.; resources, Z.Z.; data curation, Z.Z.; writing—original draft preparation, Z.Z.; writing—review and editing, L.S.; supervision, L.S.; project administration, L.S. funding acquisition, L.S. All authors have read and agreed to the published version of the manuscript.

**Funding:** This work was supported by the National Natural Science Foundation of China (No. 51875190, 52205354), National Key R&D Program of China (No. 2020YFB2007600) and the China Postdoctoral Science Foundation (No. 2022M711111).

**Institutional Review Board Statement:** Not applicable.

**Informed Consent Statement:** Not applicable.

**Data Availability Statement:** Data sharing is not applicable.

**Conflicts of Interest:** The authors declare no conflict of interest.

## References

1. Sabel, C.F.; Victor, D.G. Governing global problems under uncertainty: Making bottom-up climate policy work. *Clim. Change* **2015**, *144*, 15–27. [CrossRef]
2. Allachi, H.; Chaouket, F.; Draoui, K. Protection against corrosion in marine environments of AA6060 aluminium alloy by cerium chlorides. *J. Alloys Compd.* **2010**, *491*, 223–229. [CrossRef]
3. Luo, G.; Xiao, H.; Li, S.; Wang, C.; Zhu, Q.; Song, L. Quasi-continuous-wave laser surface melting of aluminium alloy: Precipitate morphology, solute segregation and corrosion resistance. *Corros. Sci.* **2019**, *152*, 109–119. [CrossRef]
4. Bandeira, R.M.; van Drunen, J.; de Souza Ferreira, F.A.; Rodrigues-Filho, U.P.; Tremiliosi-Filho, G. Chemically synthesized polyaniline/polyvinyl chloride blended coatings for the corrosion protection of AA7075 aluminum alloy. *Corros. Sci.* **2018**, *139*, 35–46. [CrossRef]
5. Hikku, G.S.; Jeyasubramanian, K.; Venugopal, A.; Ghosh, R. Corrosion resistance behaviour of graphene/polyvinyl alcohol nanocomposite coating for aluminium-2219 alloy. *J. Alloys Compd.* **2017**, *716*, 259–269. [CrossRef]
6. El-Etre, A.Y. Inhibition of aluminum corrosion using Opuntia extract. *Corros. Sci.* **2003**, *45*, 2485–2495. [CrossRef]
7. Zhang, X.; Wang, R.; Long, F.; Zhou, T.; Hu, W.; Liu, L. Durable superhydrophobic coating derived from hard-soft technology with enhanced anticorrosion performance. *Corros. Sci.* **2021**, *193*, 109889. [CrossRef]
8. Xun, X.; Wan, Y.; Zhang, Q.; Gan, D.; Hu, J.; Luo, H. Low adhesion superhydrophobic AZ31B magnesium alloy surface with corrosion resistant and anti-bioadhesion properties. *Appl. Surf. Sci.* **2020**, *505*, 144566. [CrossRef]
9. Mousavi, S.M.A.; Pitchumani, R. A study of corrosion on electrodeposited superhydrophobic copper surfaces. *Corros. Sci.* **2021**, *186*, 109420. [CrossRef]
10. Wang, H.; Zhu, Y.; Hu, Z.; Zhang, X.; Wu, S.; Wang, R.; Zhu, Y. A novel electrodeposition route for fabrication of the superhydrophobic surface with unique self-cleaning, mechanical abrasion and corrosion resistance properties. *Chem. Eng. J.* **2016**, *303*, 37–47. [CrossRef]
11. Liu, C.; Su, F.; Liang, J. Facile fabrication of a robust and corrosion resistant superhydrophobic aluminum alloy surface by a novel method. *RSC Adv.* **2014**, *4*, 55556–55564. [CrossRef]
12. Latthe, S.S.; Terashima, C.; Nakata, K.; Sakai, M.; Fujishima, A. Development of sol–gel processed semi-transparent and self-cleaning superhydrophobic coatings. *J. Mater. Chem. A* **2014**, *2*, 5548–5553. [CrossRef]
13. Wang, P.; Li, T.; Zhang, D. Fabrication of non-wetting surfaces on zinc surface as corrosion barrier. *Corros. Sci.* **2017**, *128*, 110–119. [CrossRef]

14. Shen, P.; Uesawa, N.; Inasawa, S.; Yamaguchi, Y. Characterization of flowerlike silicon particles obtained from chemical etching: Visible fluorescence and superhydrophobicity. *Langmuir* **2010**, *26*, 13522–13527. [CrossRef]
15. Trdan, U.; Hočevar, M.; Gregorčič, P. Transition from superhydrophilic to superhydrophobic state of laser textured stainless steel surface and its effect on corrosion resistance. *Corros. Sci.* **2017**, *123*, 21–26. [CrossRef]
16. Radwan, A.B.; El-Hout, S.I.; Ibrahim, M.A.M.; Ismail, E.H.; Abdullah, A.M. Superior Corrosion and UV-Resistant Highly Porous Poly(vinylidene fluoride-co-hexafluoropropylene)/alumina Superhydrophobic Coating. *ACS Appl. Polym. Mater.* **2022**, *4*, 1358–1367. [CrossRef]
17. Sarkar, M.K.; Bal, K.; He, F.; Fan, J. Design of an outstanding super-hydrophobic surface by electro-spinning. *Appl. Surf. Sci.* **2011**, *257*, 7003–7009. [CrossRef]
18. Ma, Q.; Tong, Z.; Wang, W.; Dong, G. Fabricating robust and repairable superhydrophobic surface on carbon steel by nanosecond laser texturing for corrosion protection. *Appl. Surf. Sci.* **2018**, *455*, 748–757. [CrossRef]
19. Vorobyev, A.Y.; Guo, C. Direct femtosecond laser surface nano/microstructuring and its applications. *Laser Photonics Rev.* **2013**, *7*, 385–407. [CrossRef]
20. Song, Y.; Wang, C.; Dong, X.; Yin, K.; Zhang, F.; Xie, Z.; Chu, D.; Duan, J. Controllable superhydrophobic aluminum surfaces with tunable adhesion fabricated by femtosecond laser. *Opt. Laser Technol.* **2018**, *102*, 25–31. [CrossRef]
21. Rukosuyev, M.V.; Lee, J.; Cho, S.J.; Lim, G.; Jun, M.B.G. One-step fabrication of superhydrophobic hierarchical structures by femtosecond laser ablation. *Appl. Surf. Sci.* **2014**, *313*, 411–417. [CrossRef]
22. Yuan, G.; Liu, Y.; Ngo, C.V.; Guo, C. Rapid fabrication of anti-corrosion and self-healing superhydrophobic aluminum surfaces through environmentally friendly femtosecond laser processing. *Opt. Express* **2020**, *28*, 35636–35650. [CrossRef]
23. Wong, T.S.; Kang, S.H.; Tang, S.K.; Smythe, E.J.; Hatton, B.D.; Grinthal, A.; Aizenberg, J. Bioinspired self-repairing slippery surfaces with pressure-stable omniphobicity. *Nature* **2011**, *477*, 443–447. [CrossRef] [PubMed]
24. Kim, P.; Kreder, M.J.; Alvarenga, J.; Aizenberg, J. Hierarchical or not? Effect of the length scale and hierarchy of the surface roughness on omniphobicity of lubricant-infused substrates. *Nano Lett.* **2013**, *13*, 1793–1799. [CrossRef] [PubMed]
25. Trdan, U.; Sano, T.; Klobčar, D.; Sano, Y.; Grum, J.; Šturm, R. Improvement of corrosion resistance of AA2024-T3 using femtosecond laser peening without protective and confining medium. *Corros. Sci.* **2018**, *143*, 46–55. [CrossRef]
26. Ahmmed, K.M.T.; Grambow, C.; Kietzig, A.-M. Fabrication of micro/nano structures on metals by femtosecond laser micromachining. *Micromachines* **2014**, *5*, 1219–1253. [CrossRef]
27. Fan, P.; Bai, B.; Jin, G.; Zhang, H.; Zhong, M. Patternable fabrication of hyper-hierarchical metal surface structures for ultrabroadband antireflection and self-cleaning. *Appl. Surf. Sci.* **2018**, *457*, 991–999. [CrossRef]
28. Saleema, N.; Sarkar, D.K.; Paynter, R.W.; Chen, X.G. Superhydrophobic aluminum alloy surfaces by a novel one-step process. *ACS Appl Mater Interfaces* **2010**, *2*, 2500–2502. [CrossRef]
29. Wang, P.; Lu, Z.; Zhang, D. Slippery liquid-infused porous surfaces fabricated on aluminum as a barrier to corrosion induced by sulfate reducing bacteria. *Corros. Sci.* **2015**, *93*, 159–166. [CrossRef]
30. Lee, J.-M.; Kim, S.J.; Kim, J.W.; Kang, P.H.; Nho, Y.C.; Lee, Y.-S. A high resolution XPS study of sidewall functionalized MWCNTs by fluorination. *J. Ind. Eng. Chem.* **2009**, *15*, 66–71. [CrossRef]
31. Wenzel, R.N. Resistance of solid surfaces to wetting by water. *Ind. Eng. Chem.* **1936**, *28*, 988–994. [CrossRef]
32. Cassie, A.B.D.; Baxter, S. Wettability of porous surfaces. *Trans. Faraday Soc.* **1944**, *40*, 546–551. [CrossRef]
33. Brug, G.J.; Van Den Eeden, A.L.G.; Sluyters-Rehbach, M.; Sluyters, J.H. The analysis of electrode impedances complicated by the presence of a constant phase element. *J. Electroanal. Chem. Interfacial Electrochem.* **1984**, *176*, 275–295. [CrossRef]
34. Zhang, X.-F.; Chen, Y.-Q.; Hu, J.-M. Robust superhydrophobic $SiO_2$/polydimethylsiloxane films coated on mild steel for corrosion protection. *Corros. Sci.* **2020**, *166*, 108452. [CrossRef]
35. Shi, H.; Han, E.-H.; Liu, F. Corrosion protection of aluminium alloy 2024-T3 in 0.05M NaCl by cerium cinnamate. *Corros. Sci.* **2011**, *53*, 2374–2384. [CrossRef]